RESEARCH

RESEARCH: Original Research

ELSEVIER

Rational design of thermally stable polymorphic layered cathode materials for next generation lithium rechargeable batteries

Xiao Li [1,4,#], Qingwen Gu [1,#], Bao Qiu [1,4,*], Chong Yin [1], Zhining Wei [1], Wen Wen [3], Yibin Zhang [1], Yuhuan Zhou [1,4], Han Gao [1,4], Haoyan Liang [1], Zhilong He [1], Minghao Zhang [2,*], Ying Shirley Meng [2,5,*], Zhaoping Liu [1,4,*]

[1] Ningbo Institute of Materials Technology & Engineering (NIMTE), Chinese Academy of Sciences, Ningbo 315201, PR China
[2] Department of NanoEngineering, University of California San Diego (UCSD), La Jolla, CA 92093, USA
[3] Shanghai Synchrotron Radiation Facility, Chinese Academy of Sciences, Zhangjiang High-Tech. Park, Pudong New Area, Shanghai 201204, PR China
[4] Center of Materials Science and Optoelectronics Engineering, University of Chinese Academy of Sciences (UCAS), Beijing 100049, PR China
[5] Pritzker School of Molecular Engineering, University of Chicago, Chicago, IL 60637, USA

Classical layered transition metal oxides have remained the preferred cathode materials for commercial lithium-ion batteries. Variation in the transition metal composition and local ordering can greatly affect the structure stability. In classical layered cathodes, high concentrations of electrochemically inert Mn elements usually act as a pillar to stabilize the structure. When excess amount of Li and Mn are present in the layered structure, the capacity of the Li-rich layered oxide (molar ratio of lithium over transition metal is larger than one by design) can exceed that expected from transition metal redox. However, the over lithiation in the classical layered structure results in safety issues, which remains challenging for the commercialization of Li-rich layered oxides. To characterize the safety performance of a series of Li-rich layered cathodes, we utilize differential scanning calorimeter and thermal gravimetric analysis; this is coupled with local structural changes using *in situ* temperature dependent synchrotron X-ray diffraction and X-ray adsorption spectroscopy. These methods demonstrate that the gradual decrease of the Mn–M (M = Ni, Co, Mn and Li) coordination number directly reduces structural stability and accelerates oxygen release. For safety characterization tests in practice, we evaluate the thermal runaway process through accelerating rate calorimeter in 1.0 Ah pouch cells to confirm this trend. Using the insights obtained in this work, we design a polymorphic composition to improve the thermal stability of Li-rich layered cathode material, which outperforms Ni-rich layered oxides in terms of both electrochemical and safety performances.

Keywords: Li-ion batteries; Li-rich layered cathode; Thermal stability; Local structure modulation; Polymorphic composition design

Introduction

Lithium-ion batteries (LIBs) are playing increasingly important roles in powering electric vehicles with high energy density [1–3]. However, the safety of state-of-the-art LIBs is contingent on their energy density. As a safety-determining component, it is

necessary to ameliorate the thermal performance of cathode materials that are characterized by structural decomposition and transformation. The oxygen released during the structural decomposition is notably detrimental due to the immense heat generation in organic electrolytes [4]. One of the key considerations for manufacturing high-security LIBs is thus to impede structural transformation and oxygen release of cathode materials under the increased temperature. Starting with the commercialization of $LiCoO_2$ based LIBs, layered oxides have remained the preferred cathode material for commercial LIBs. Classical layered cathode materials $LiNi_xCo_yMn_zO_2$ (NCM, x + y + z = 1) show a higher structural stability and a lower level of oxygen release with the increase of inert Mn^{4+} concentrations [4], which was attributed to the strong Mn–O covalence. Modification strategies, such as core–shell [5] or concentration gradient [6,7] structures were thus adopted to enable Mn-rich environment on the classical layered materials' surface to further improve their thermal stability [8,9]. However, the energy density of these classical layered materials is limited by both their lithium content and the extraction of one electron per transition metal (TM) ion.

The limitations of classical layered cathodes can be overcome in Li-rich cathode systems with the formula of $xLi_2MnO_3 \cdot (1 - x)$ $LiTMO_2$. Li-rich layered NCM materials are usually considered as the nanocomposites of Li_2MnO_3-like components and $LiTMO_2$ (TM = Mn, Ni, Co) components [10]. Within the TM layer of the Li_2MnO_3-like component, Li and TM ions form a honeycomb superstructure where Li sits at the center of each hexagon, which is referred as $LiMn_6$ ordering [11]. This local ordering necessarily leads to more Li–O–Li configurations and, as a consequence, more potentially labile oxygen electrons for electrochemical reactions [12]. This family of materials has shown superior energy density, almost two times that of $LiCoO_2$ [10]. Recent works have also demonstrated that anion (oxygen) redox in these materials is the main reason for the high reversible capacity over 300 mAh g^{-1} at room temperature [13–15].

In Li-rich layered NCM materials, the proportion of Mn element in total TM is over 50%, which is believed to have an exceptional thermal stability based on the composition design rule for classical layered materials. However, this hypothesis neglects the different effects of Mn on oxygen in terms of local coordination environment. When excess Li cations are incorporated into the lattice, the presence of the distinct $LiMn_6$ ordering in the TM layer results in the formation of the uncoordinated O_{2p} orbitals [12,16]. Although this unique local ordering activates oxygen redox involving O-dominated states at high voltage, the delithiated cathode shows worse stability than that of classical layered oxides without oxygen-redox activation [17]. With the elevation of electrochemically activated oxygen redox, the onset temperature of oxygen release gradually decreases as confirmed by thermal desorption spectrometry-mass spectrometry [18,19]. Apart from oxygen release, the structural change at an elevated temperature is another factor that determines the thermal stability. In contrast to the layered-to-spinel transformation in Ni-rich layered cathodes, the charged Li-rich and Mn-rich layered cathodes display a local structure distortion [20]. Decreasing Mn concentration helps mitigate oxygen release from Li-rich layered materials, however, this improved structural stability is achieved at the expense of the capacity or energy density [19].

Under this circumstance, concentration gradient [21] or core–shell [22] structures with decreased Mn content from bulk to surface have been proposed to optimize their thermal performance while maintain high energy density. These results provide insights into the rational design of Li-rich layered materials with a balance between energy density and thermal stability. These works studied the thermal stability of charged Li-rich layered materials in terms of self-heating temperature [17,23], oxygen release [18,19], and structural transformation [20,21]. The underlying principles remain elusive for predicting the thermal stability of lithium-rich layered oxides and designing the materials' composition or structure to further improve the thermal stability.

In this work, we conduct a systematic study on the thermal stability of a series of Li-rich layered cathode materials, with a nominal formula of $Li_{1+Y}[Ni_{2/(3+3X)}Co_{2/(3+3X)}Mn_{2X/(3+3X)}]O_2$ (LR-NCM11X: X = 2, 3, 4, 6; Y > 0) in the perspective of the local coordination of Mn elements. We employed differential scanning calorimeter (DSC), and thermal gravimetric analysis coupled with mass spectrometry (TG-MS) to evaluate their safety performance. *In situ* temperature-dependent synchrotron X-ray diffraction (TD-SXRD) and *ex situ* X-ray adsorption spectroscopy (XAS) were also performed to detect onset temperatures of phase transitions and the local structure environments after electrochemical cycling. The extended X-ray absorption fine structure (EXAFS) results exhibit the changes of the coordination environments of Mn elements at different states that directly determine the thermal stability of the layered materials. These results confirm that more Mn content in the Li-rich layered cathode materials could contribute to a higher capacity but results in a larger reduction of the thermal stability. The similar trend of thermal runway is also observed in practical batteries monitored by accelerating rate calorimeter (ARC) with 1.0 Ah pouch cells. These findings elucidate the dependence of thermal stability on Mn coordination environments, which can serve as a rational guide to design a polymorphic Li-rich layered cathode with improved reliability.

Material and methods

Materials synthesis

The detailed procedures of material preparation are similar to those in our previous report [13]. The carbonate precursors were prepared by co-precipitation method: stoichiometric amounts (Ni: Co: Mn = 1:1:1, 1:1:2, 1:1:3, 1:1:4 and 1:1:6) of $NiSO_4 \cdot 6H_2O$, $CoSO_4 \cdot 7H_2O$, and $MnSO_4 \cdot 5H_2O$ were dissolved in deionized water; then the aqueous solution with the reagent concentration of 2.0 mol/L was continuously pumped into a continuous stirring tank reactor (CSTR, 250 L); at the same time, Na_2CO_3 aqueous solution (2.0 mol/L) and NH_4OH aqueous solution (0.2 mol/L) were pumped into the CSTR, separately. During the reaction, the pH was kept at around 8.0 and the temperature was kept at 60 °C. The as-obtained co-precipitation powders were filtered, washed several times with deionized water, and then dried at 120 °C overnight. After mixing Li_2CO_3 (with the designed Li to TM ratio of 1.0, 1.2, 1.3, 1.4, 1.5, respectively), the precursors were pretreated at 500 °C for 5 h before calcining at 820 °C for 12 h in air. The as-obtained materials were $Li_{1.000}Ni_{0.333}Co_{0.333}$-

$Mn_{0.333}O_2$ (NCM111), $Li_{1.079}Ni_{0.225}Co_{0.225}Mn_{0.449}O_2$ (LR-NCM112), $Li_{1.106}Ni_{0.170}Co_{0.170}Mn_{0.511}O_2$ (LR-NCM113), $Li_{1.143}Ni_{0.136}Co_{0.136}Mn_{0.544}O_2$ (LR-NCM114) and $Li_{1.171}Ni_{0.098}Co_{0.098}Mn_{0.585}O_2$ (LR-NCM116).

Polymorphic materials

To obtain polymorphic Li-rich layered materials, the LR-NCM112 and LR-NCM114 precursors which have mentioned in detail above were blended uniformly with a ratio of 4: 6. Then the polymorphic precursors were mixed uniformly with Li_2CO_3, where the designed Li to TM ratio was 1.3. The mixture was pre-calcinated at 500 °C for 5 h, followed by calcinated at 820 °C for 12 h. After cooling down to room temperature naturally, the polymorphic LR-NCM113 were obtained.

Electrochemical measurements

To obtain cathode electrode, active materials were mixed with super P carbon, and polyvinylidene fluoride (PVDF) binder with a ratio of 2.5%: 2.5%: 95%, and the compounds were removed in N-methyl-2-pyrrolidinone (NMP). After stirring for 12 h, the slurries were coated on the collector aluminum foil uniformly by using a stainless- steel scraper, followed by drying at 80 °C for 4 h. The final circular electrode was used to assemble coin-type 2032 cells with Celgard 2502 separator, Li metal foil, and electrolyte which composed ethylene and dimethyl carbonate (3:7 volume ratio) with $LiPF_6$ (1.0 M) in an argon-filled glove box. The cells were performed a galvanostatic charge test: charging to the potential of 4.8 V vs Li^+/Li^0 at 25 mA g^{-1} current density. Then the overcharged cells were disassembled in a glove box before the charged electrode washed several times using DMC solvent. The charged cathode powders were obtained by scratching away the electrode from the current collector.

In the pouch batteries configuration, the negative electrodes consist of 94.5 wt.% graphite (Gr), 2 wt.% styrene butadiene rubber (SBR), 1 wt.% SP, 1 wt.% KS-6, and 1.5 wt.% aqueous binder (CMC). The positive electrodes were prepared with 92.86 wt.% active materials, 0.14 wt.% single wall carbon nanotubes (SWCNTs), 4 wt.% poly(vinylidene) (PVDF), 2 wt.% Super-P, and 1 wt.% carbon nanotube (CNT). The positive electrodes were tailored into 53 mm in length and 43 mm in width. Then 1Ah pouch batteries were assembled in a clean room, during which 3.5 g commercial electrolyte was used. The pouch batteries were charged to 4.65 V at 100 mA g^{-1} current density in LAND-CT2001A battery tester at room temperature (25 °C).

Atomic structure, morphology, and composition characterizations

HAADF-STEM (Spectra 300, FEI) imagines were obtained by using double spherical aberration-corrected Spectra 300 electron microscopes operated at 300 kV using a convergence semi-angle of 24.9 mrad for direct observations on atomic arrangements of PLR-NCM113 and HLR-NCM113 samples. The morphology and atomic composition of primary particle was identified firstly using energy dispersive spectrometer (EDS). The atomic ratio of Mn, Co, Ni is almost 2:1:1 and 4:1:1 corresponds to LR-NCM 112 and LR-NCM114 compositions of PLR-NCM113. SEM (Quanta FEG250, FEI) measurement was conducted to observe the morphology of secondary particles in PLR-NCM113. The atomic composition and distribution were also detected using energy dispersive spectrometer (EDS) simultaneously. The PLR-NCM113 powders were smeared to the conducting resin evenly. Chemical analyses of element amounts were measured using ICP-OES (Optima 2100, PerkinElmer).

DSC measurements

The DSC measurement was conducted with DSC 8000 (Perkin Elmer). The temperature range was from room temperature to 450 °C with a heating rate of 10 °C/min. The charged cathode powders have mentioned in in situ Temperature-resolved SXRD test, and then transferred into a stainless-steel crucible, followed by dropping in electrolyte. To reduce the oxygen and water contamination, the adding and sealing process were performed in the glovebox. The ratio of cathode and electrolyte was 1:1 by weight.

TG-MS test protocol

The TG-MS test was used to characterize the thermal properties and gaseous products of the cell components. The experiments were performed on TGA8000-Clarus SQ8T (Perkin Elmer). The cathode electrode acquired by disassembling coin-type 2032 cells was firstly washed with DMC to remove the adsorbed electrolyte, and then the cathode powders were scratched from the electrodes in an argon-filled glove box and then dried at room temperature in the same glove box. All the samples were pressed in an aluminum crucible in the glove box and heated from 50 °C to 600 °C at a heating rate of 10 °C min^{-1} in a highly pure flowing argon atmosphere.

In situ TD-SXRD

SXRD patterns were collected at the beamline BL14B of the Shanghai Synchrotron Radiation Facility (SSRF) with the X-ray wavelength of 0.6887 Å. For the charged samples, the initial charge coin cells were transferred to a glove box for disassembly. The cathodes were washed in DMC solvent in the glove box and the mixed cathode powders (including the binder and conductive carbon) were obtained by scratching away the electrode from the current collector. Then they were loaded into 1.0 mm diameter corundum capillaries. The capillary then was mounted on the thermal stage of beamline 14B1, at Shanghai Synchrotron Radiation Facility (SSRF). The wavelength used at the 14B1 was 0.6887 Å (18 KeV). To track the structural changes during thermal degradation, SXRD spectra continuously were recorded as a set of circles on a two-dimensional image plate detector in the transmission mode during heating from room temperature to 400 °C (i. e. heating rate = 5 °C min^{-1}). The total recording time for one spectrum was approximately 30 s.

Hard XAS

The hard XAS experiments with transmission mode were performed using the BL11B beamline in the SSRF at Shanghai, China. The standard comparison sample, Ni, Co, and Mn foils were measured simultaneously. The X-ray absorption near edge structure (XANES) data and extended X-ray absorption fine structure (EXAFS) data were processed and fitted using the ATHENA software package [24]. (More detailed). The ATHENA software package was employed to process and fit the X-ray absorption

near edge structure (XANES) data and extended X-ray absorption fine structure (EXAFS) data.

ARC test protocol

The accelerated rate calorimetry (ARC-EV+) instrument manufactured by Thermal Hazard Technology was used to evaluate the thermal runaway features. The heat-wait-seek method was conducted on the ARC to detect the adiabatic self-heating rate as a function of time. The starting temperature was 40 °C with a heating step of 5 °C. The detected self-heating rate was 0.02 °C/min and the waiting time was 40 min.

Results and discussion

Bulk structure and electrochemical performances

A series of Li-rich layered materials $Li_{1.079}Ni_{0.225}Co_{0.225}Mn_{0.449}O_2$ (LR-NCM112), $Li_{1.106}Ni_{0.170}Co_{0.170}Mn_{0.511}O_2$ (LR-NCM113), $Li_{1.143}Ni_{0.136}Co_{0.136}Mn_{0.544}O_2$ (LR-NCM114) and $Li_{1.171}Ni_{0.098}Co_{0.098}Mn_{0.585}O_2$ (LR-NCM116), and a comparison sample $Li_{1.000}Ni_{0.333}Co_{0.333}Mn_{0.333}O_2$ (NCM111) were synthesized via the co-precipitation method. The structural information of these materials has been revealed in detail in our recent work [25]. The most critical structural feature for Li-rich layered cathodes is the presence of the Li_2MnO_3-like domain, in which the excess lithium exists in TM layers in the form of $LiMn_6$ honeycomb ordering as confirmed by SXRD *Rietveld* refinements (Fig. S1a-f and Table S1). Unsurprisingly, the Li proportion in TM slab increases from 1.2% to 18.0% with Mn content increasing (Fig. S1f). This implies that excess Li ions are engaged in Mn coordination environment and effectively alter the nearest cations neighbor Mn–M, M = Li, Ni, Co and Mn.

The initial charge–discharge voltage profiles of the synthesized materials are provided in Fig. 1a. The initial charge capacity increases from approximately 250 mAh g^{-1} for NCM111 to 340 mAh g^{-1} for LR-NCM116 when charged to 4.8 V vs Li$^+$/Li^0 under a constant current density of 25 mA g^{-1}. Although the charge capacities increase with higher Mn content in LR-NCM cathode materials, LR-NCM114 delivers the highest discharge capacity. After calculation on the basis of the experimental data (see Supplementary Note 1 for details), almost 90% Li$^+$ ions are extracted from the lattice for all the samples as shown in Fig. 1b, when no other side reactions are considered [23,26–28]. This estimation can well exclude the effect of the lithium content on the thermal stability of the delithiated Li-rich layered cathodes. Note the lithium concentration can vary obviously for classical layered cathodes with different compositions when charged to the same voltage [28]. The charging capacity difference of the studied samples originates from the oxygen redox which corresponds to the plateau region starting around 4.45 V vs Li$^+$/Li^0[29]. We then selected 4.45 V vs Li$^+$/Li^0 as a cut-off voltage to distinguish the oxygen redox (above) and the TM redox (below) [29]. Fig. 1c exhibits an obvious rising tendency for an oxygen redox capacity with a higher content of Mn in the layered structure. The activated oxygen can lead to an undesirable oxygen environment, accelerating structure evolution and deteriorating cathode performance in terms of stability and safety.

Thermal stability, oxygen gas release, and structure transformation

To investigate the thermal stability, DSC was performed on these charged materials with the cutoff voltage of 4.8 V vs Li$^+$/Li^0. It is
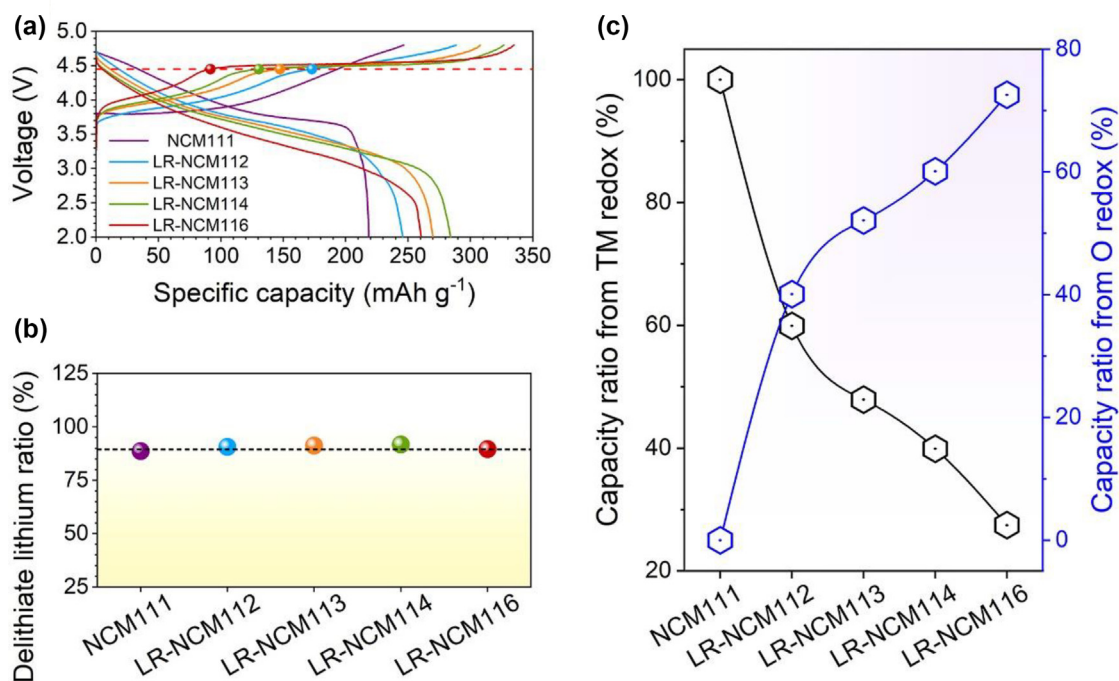

FIGURE 1

Comparison of electrochemical performances of different cathode materials. (a) Galvanostatic initial charge–discharge profiles of these cathode materials under the current density of 25 mA g^{-1}. (b) Comparison of extracted lithium ratio holding at the same voltage for these cathode materials. (c) Measured oxygen redox capacity above 4.45 V.

well acknowledged that the enormous amount of heat caused by the exothermic reaction of oxygen and organic electrolytes jeopardizes the safety of Li-ion batteries [30]. To mimic the exact battery environment, all the charged powders (9 mg) directly contacted with the organic electrolyte (7 μL) while heating. The detailed procedures are described in Experimental section. As can be observed in Fig. 2, all the charged materials exhibit similar behaviors containing a strong exothermic peak and several weak peaks prior to the strong peak. The exothermic reactions appearing at lower temperature can come from three processes: (1) structural transition of active materials due to the TM migration [31]; (2) the decomposition of the conventional organic electrolyte [32,33]; (3) the redox reaction between the electrophilic alkyl carbonate solvents in electrolyte and the nucleophilic superoxide or peroxide species formed by electrolyte oxidation [12,34]. The strongest peak is ascribed to the intense reaction between O_2 and electrolyte, which would generate tremendous heat that could ignite the thermal runaway of batteries [26,35,36]. This peak temperature is 284 °C, 256 °C, 251 °C, 241 °C and 229 °C for NCM111, LR-NCM112, LR-NCM113, LR-NCM114, LR-NCM116, respectively. Moreover, the total amount of heat release is also quantified for evaluating the thermal stability of these cathode materials. The thermal release enlarges from 1218.24 J g^{-1} (NCM111) to 1597.56 J g^{-1} (LR-NCM116). These results indicate that when more Mn and Li participate in the electrochemical reactions, it is detrimental to the thermal stability of Li-rich layered cathode materials.

It is commonly acknowledged that oxygen gas release is one of the most important factors to cause the thermal instability of delithiated layered cathode materials [37,38]. Therefore, TG-MS was implemented to monitor the onset temperature and amount of oxygen release. As shown in Fig. 3a-b, little difference is observed on the onset temperature between weight loss and oxygen release for each sample, which implies that the oxygen gas results from the decomposition of cathode materials. It is

obvious that as the Mn content increases, the onset temperature of oxygen release gradually decreases (Fig. 3b). These results indicate that the charged Li-rich layered cathode materials containing more Mn show inferior structural stability because of the poor stability of lattice oxygen [27].

In addition to oxygen release, the layer-to-spinel-to-rocksalt phase transition at elevated temperature is also closely related to the thermal stability of cathode materials [4,39]. As one powerful tool to analyze structure transitions during heating, *in situ* TD-SXRD was employed in this work. Fig. 3c-d present the contour plots of SXRD patterns at selected 2θ ranges within the temperatures from 30 °C to 400 °C for all delithiated cathode samples. The SXRD patterns in the whole 2θ range are also provided in Figs. S2–S6. According to previous studies [26,40,41], oxygen release inevitably reduced the average oxidation state of TM ions (most likely for Ni^{4+}) during heating. The reduced TM cations often show smaller activation barriers for migration [35,42], which facilitates TM cations migrating from original octahedral sites to the neighboring octahedral lithium vacancies by hopping intermediate face-sharing tetrahedral sites. In general, the layered structure $(003)_R$ diffraction peak and $(018)_R$/$(110)_R$ pairs can be considered as a signature to trace the TM ions migration process [27]. To be specific, with more TM ions migration, the $(003)_R$ peak disappears gradually while the $(018)_R$/$(110)_R$ pairs begin to coalesce. As shown in Fig. 3c-d, all the delithiated samples show a similar structural transition from the ordered layered structure to a disordered spinel phase during heating. The peaks $(003)_R$ in Fig. 3c shift to a lower 2θ slowly at first due to the thermal expansion of materials, followed by moving to a higher angle along with the peaks fading at an increasing temperature. Moreover, the $(018)_R$ and $(110)_R$ peaks starts to merge after thermal expansion (Fig. 3d). The turning point of peaks showing different behaviors can be regarded as the onset temperature of structural decomposition. The onset temperatures of the delithiated cathode materials present a decreasing trend
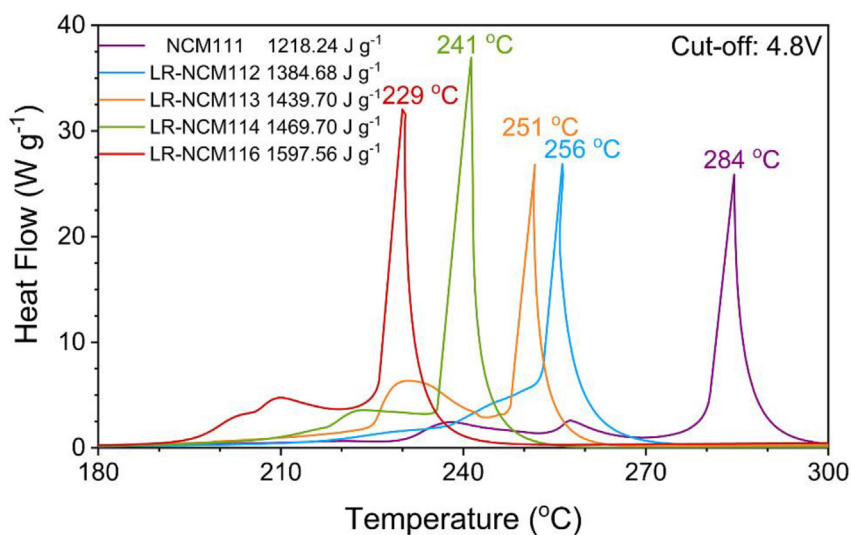

FIGURE 2

Thermal stability for charged cathode materials. DSC profiles of the delithiated samples with a scanning rate of 1 °C min^{-1}. The cells were charged using constant-current to 4.8 V *vs* Li$^+$/Li before disassembling. The obtained cathode powders were mixed with electrolyte in a certain proportion (1:1 by weight) for the DSC testing.
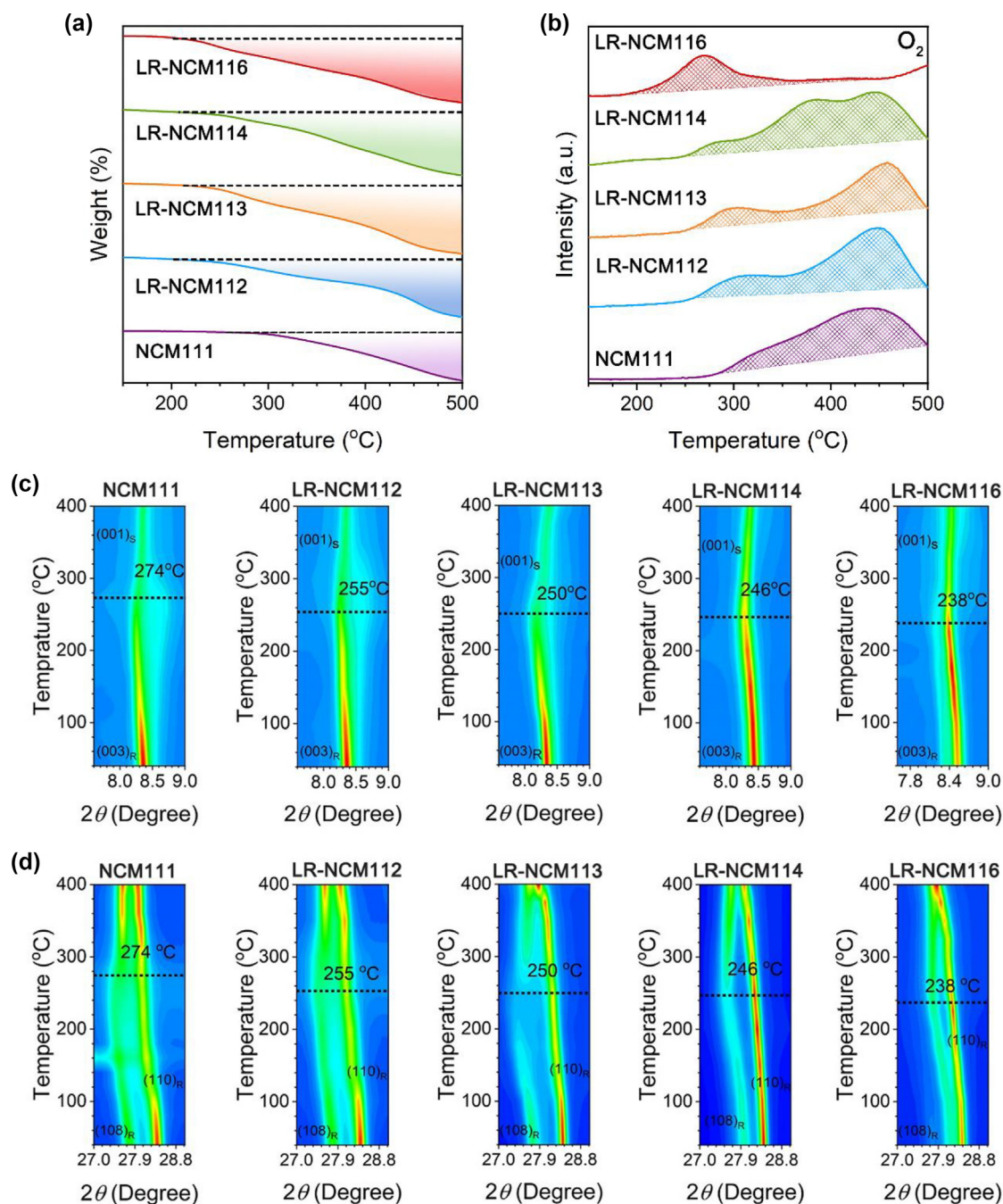
FIGURE 3

Oxygen release and structural changes at elevated temperature in different cathode materials. (a) TG analysis of the delithiated cathodes with a heating rate of 5 °C min^{-1}. (b) *In situ* oxygen release at different temperature determined by MS. (c-d) The contour plots of SXRD patterns for (c) $(003)_R$ diffraction peak, (d) $(108)_R$ and $(110)_R$ diffraction peaks within temperatures from 25 °C to 400 °C. The low temperature for oxygen release and structure change reflects a poor thermal stability.

with the Mn content increasing, from 274 °C (NCM111) to 238 °C (LR-NCM116). Although the temperature from our SXRD has a slight difference from the data obtained by MS and DSC, they all show the similar trend. More importantly, the decreased temperatures of the phase transitions agree well with the oxygen evolution and exothermic peaks for these delithiated samples, which manifests the inferior thermal stability of Li- and Mn-rich layered oxides.

The above analysis reveals that Mn plays a different role in safety performance for Mn-based Li-rich layered cathodes and Ni-based classical layered cathodes, which results from the different interactions between Mn and O. The safety of cathode can thus be tailored by regulating local environments (especially on Mn). The dominating oxygen stability, determined by the circumambient Mn ions, accounts for their thermal performance. It is critical to further study how the Mn local coordination environment evolves in charged cathodes and how these changes results in the thermal instability. To answer these questions, we deployed XAS to explore the underlying mechanism for the poor thermal stability of delithiated Li-rich layered cathode materials.

Characterizations of local structure by XAS

Mn K-edge XANES for the pristine, charged to 4.8 V and 300 °C heated cathode materials are shown in Fig. 4a–c, respectively. No obvious shift of Mn K-edge peak is observed (Fig. S7), which implies the same Mn^{4+} oxidation state at all states according to the previous research [43]. Further information about local coordination around Mn-sites in all samples is provided by EXAFS spectra (Fig. 4d–f). The EXAFS spectra show a typical first shell (bond length at 1.5 Å) corresponding to Mn coordinated by 6 oxygen atoms and a second shell (bond length at 2.4 Å) associated with the Mn–TM scattering. Note that Mn–Li scattering has a negligible contribution to the second shell feature due to
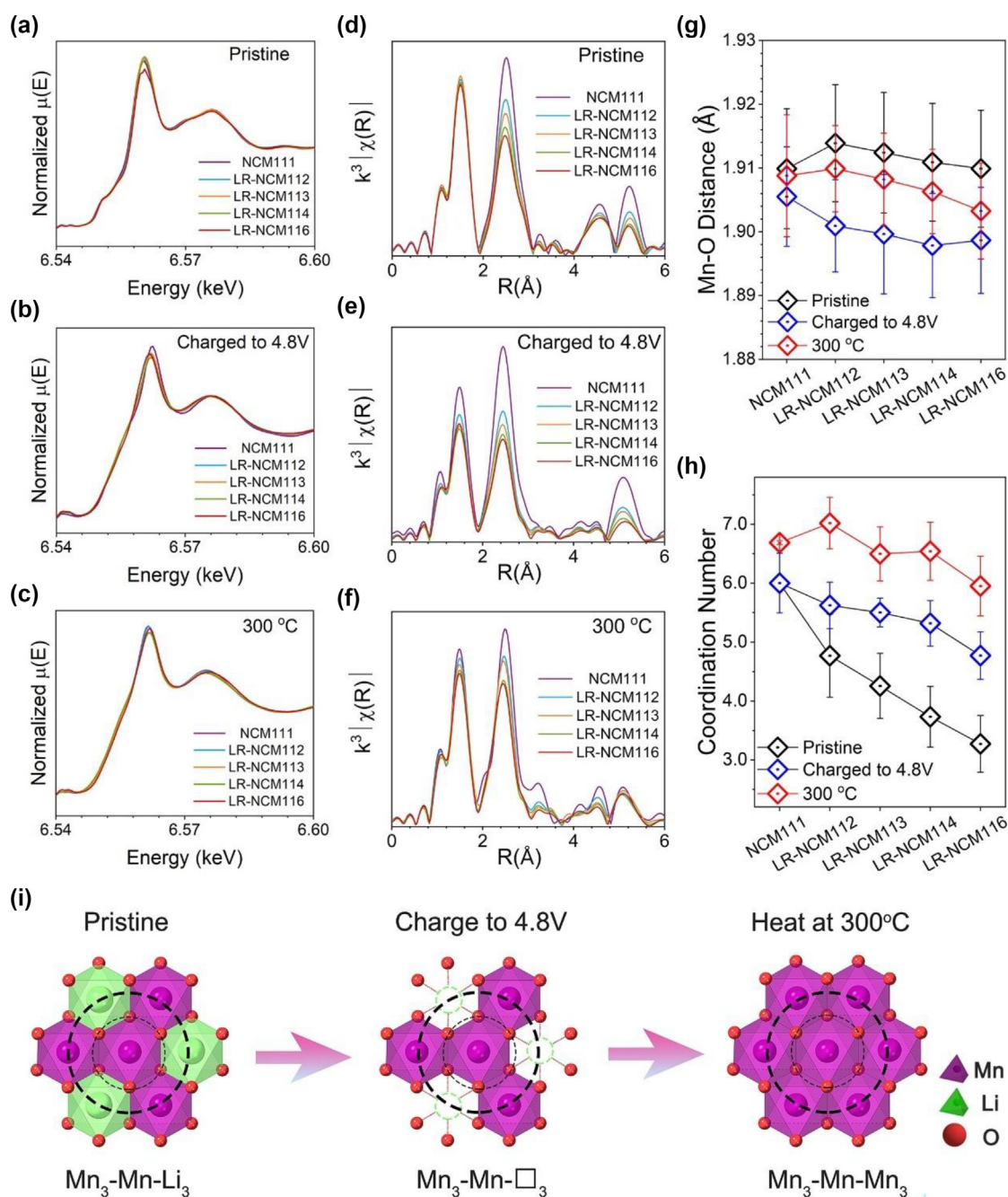

FIGURE 4

Characterization of Mn coordination environment in different cathode materials. (a–c) K-edge XANES spectra of Mn for (a) pristine, (b) charged to 4.8 V, and (c) 300 °C-heated samples. (d–f) K-edge EXAFS spectra of Mn for (d) pristine, (e) charged to 4.8 V, and (f) 300 °C-heated samples. (g–h) Mn-O distance for the first Mn–O shells (g) and coordination numbers of Mn for the second Mn–M shells (h) obtained based on the fitting of the EXAFS spectra. The first peak in EXAFS spectra at lower radical refers to the Mn–O coordination and the second peak at higher radical involved the Mn–M coordination, where M can be occupied by Ni, Co, Mn, and Li. The high Debye–Waller factor represents a disordered Mn–O pairs while the decreasing coordination for Mn indicates Mn coordinates with more light Li atoms. (i) Schematic diagram of Mn local structure after the coordination environments change at different states of cathode materials.

the less extranuclear electrons. Some weak peaks in long range (longer than 2.4 Å) arise from the further atoms scattering, and the other peaks in short range (shorter than 1.0 Å) originate from the incomplete Fourier transform due to the restricted k space in a real sample. The intensity of the first Mn–O shell remains almost unchanged for the pristine state of all samples, but decreases for the delithiated and heated samples, implying the serious distortion of Mn–O bond [44]. Given the highest proportion, Mn plays a crucial role in thermal stability in terms of Mn–O covalence, which is determined by the hybridization between Mn 3d orbitals and O 2p orbitals as indicated by Mn–O bond distance [45]. To quantify the Mn environment changes after charging and heat treatment, EXAFS fittings were implemented to reveal the first and second coordination shells of Mn (Figs. S8–S10), and the fitting results are listed in Table S2. The Mn–O bond distance was analyzed to compare the Mn–O covalence at different states (Fig. 4g). It is observed a significant Mn–O bond contraction for each Li-rich NCM composition at delithiated state. Based on the previous work [46], the Mn–O distance keeps constant in the classical NCM111 material during charging process since no charge transfer is captured from the Mn–O bonding. Generally, a shorter Mn–O bond implies a higher Mn–O covalence, which in fact results from a greater charge transfer from oxygen in Li-rich NCM materials [47–49]. In this case, the charge extraction from oxygen, namely oxygen redox, generates highly unstable oxygen species, so as to contribute to the aggravated oxygen release and poor thermal stability. After further thermal treatment, the recovery of Mn–O bond indicates the structural relaxation [40].

Since oxygen redox is responsible for the inferior thermal stability, the amount of activated oxygen can be set as a standard to compare the stability in different Li-rich layered cathodes. Given the activated oxygen existing in the form of Li-O-Li configuration [12], attention needs to be paid to the second Mn–TM shell. As illustrated in Fig. 4h, the Mn-TM coordination number decreases from 6.00 (NCM111) to 3.44 (LR-NCM116) for the pristine samples, which indicates more Li ions are involved in Mn coordination [25]. With more Li-O-Li configurations, more oxygen redox is expected to be involved in the electrochemical process that agrees well with the electrochemical performance (Fig. 1c). Among all delithiated samples, the Mn coordination number also decreases with Mn content increasing. On the basis of the trend of oxygen redox and thermal stability, it is conclusive that the more decrease of the Mn-TM coordination number and the more involvement of oxygen redox, the worse thermal stability. After heat treatment, the Mn-TM coordination number for each composition increases over 6 (Fig. 4h). For layered structure, Mn coordinates with 6 transition metal atoms at most while the Mn-TM coordination number increases to 12 in spinel/rocksalt structure. Therefore, the significant increase for Mn-TM coordination number suggests the layer-to-spinel-to-rocksalt structure transformation, agreeing well with our in situ TD-SXRD data (Fig. 3c-d). A schematic illustration of possible Mn local structure is shown to reveal its effect on the thermal stability (Fig. 4i). Note that the local structure configuration of Mn_3-Mn-Li_3 is thermodynamically stable in Li-rich layered cathode, in which Li can activate the oxygen redox in the form of Li-O-Li [12]. When charged to 4.8 V vs Li^+/Li^0, Li ions in TM layers

were extracted and the formed vacancies (denote as □) were coordinated with Mn [50]. The charge transfer process from oxygen ions contributes to the decreased oxygen stability, which can thus accelerate oxygen release and structural evolution during heat treatment.

The corresponding Co, Ni oxidation states, and local structure analysis are shown in Figs. S11–S12 together with the first and second coordination shell fitting results provided in Figs. S13–S18. As shown in Figs. S11a-c and S12a-c, there is little difference in Co and Ni K-edge position among the pristine samples (Figs. S11a and S12a), indicating the chemical oxidation states are identical for Co and Ni. When charged to 4.8 V vs Li^+/Li^0, a significant shift of Co and Ni K-edge is observed from NCM111 to LR-NCM116 indicating the different Co and Ni oxidation states among delithiated samples (Figs. S11b and S12b). A similar edge shift is observed in heated samples (Figs. S11c and S12c). Apart from the oxidation state, the coordination environments of Co and Ni are shown in Figs. S11d-f and S12d-f and further analysis was performed by EXAFS fitting (Figs. S11g, S12g and Table S3-4). Unlike the Mn–O bond, the Co-O and Ni-O bond vary in a similar trend for a certain composition at different states due to the charge transfer process, implying the same effect on thermal stability for Co (Ni) in NCM111 and Li-rich NCM cathode materials. In addition, the Co (Ni) coordination environments are similar in different compositions at the same state (Fig. S11h, S12h). Based on the above local structure analysis, we conclude that the O instability with lower Mn–M coordination number in Mn local environments is the key factor to determine the thermal stability of Li-rich layered cathode materials.

Safety analysis with ARC in pouch cells

To further confirm the impact of Mn content on thermal stability of Li-rich layered cathodes, we performed accelerating rate calorimetry (ARC) to study the thermal runaway features by simulating an adiabatic condition in practical batteries. 1-Ah pouch cells containing Li-rich layered cathodes and graphite anodes were prepared and the initial charge curves of these five batteries (charged to 4.65 V) are shown in Fig. S19. The thermal runaway properties of the prepared batteries were measured by the EV + ARC system while the open-cell voltage (OCV) was detected along with battery temperature rising. Three characteristic temperatures, T_1, T_2, and T_3, were used to describe the thermal runaway behavior of batteries [30,32,51,52]. Temperature T_1 represents the onset self-heating temperature of the battery, at which the battery's temperature increase rate reaches 0.02 °C s^{-1}. The onset self-heating results from the decomposition of the solid electrolyte interface, and the exothermic reaction usually initiates at 60–120 °C [53]. Temperature T_2 refers to the trigger temperature of the thermal runaway and it is defined when the battery's temperature increasing rate arrives to 1 °C s^{-1}. Different from a gradual temperature increase beyond T_1, the battery's temperature will rise sharply after reaching T_2. The last temperature, T_3, is defined as the maximum temperature reached by the battery during thermal runaway. The temperature difference between T_3 and T_1, denoted as ΔT, reflects the total heat generation during thermal runaway [51]. The comparison of T_1, T_2, and T_3 in pouch cells with different cathodes are shown

in Fig. 5a–f. The collected T₁ temperature at around 80 °C, corresponds to a common chemical reaction occurring at this temperature, which reflects an analogous thermal stability at a lower temperature for these five cells. As the batteries temperature further increase, the thermal runaway is triggered. Interestingly, the onset temperature, T₂, shows a decreased tendency for higher Mn content cathodes: 232.67 °C for NCM111, 224.09 °C for LR-NCM112, 200.45 °C for LR-NCM113, 195.64 °C for LR-NCM114 and 191.43 °C for LR-NCM116. Moreover, before igniting the thermal runaway, the OCV of all pouch cells descends slowly at the beginning and drops to 0 V sharply when the temperature reaches 160 °C, suggesting that the thermal runaway is not caused by the internal short circuits, in accord with the previous results [32,51]. Therefore, we infer that the major heat that contributes to the thermal runaway is generated from the redox reaction between the highly active oxygen species released from cathode and the flammable electrolyte [26] or reactive lithiated anode [32,41,51]. After T₂, battery temperature rapidly increases

to the maximum temperature T₃. An enlarged ΔT indicates more heat generation during thermal runaway, and more energy storage in the testing battery. Therefore, the battery with LR-NCM114 gets the maximum ΔT, coincides well with the maximal input energy during the initial charge process (Fig. S19).

Polymorphic materials design to improve thermal stability

Based on the above analysis, we have demonstrated that the O stability in Mn local structure is the key factor to determine the thermal stability of Li-rich layered cathode materials. As reported previously [54–57], decreasing the size of Li_2MnO_3-like domain can help improve the O stability through increasing the activation energies for the formation of oxygen vacancies and TM migration. Therefore, designing Li-rich layered cathodes with small Li_2MnO_3-like domain size is crucial to improve thermal stability. Note that Li content can affect the Li_2MnO_3-like structure significantly during synthesis [58,59]. We thus propose the design of polymorphic cathode materials by using two different
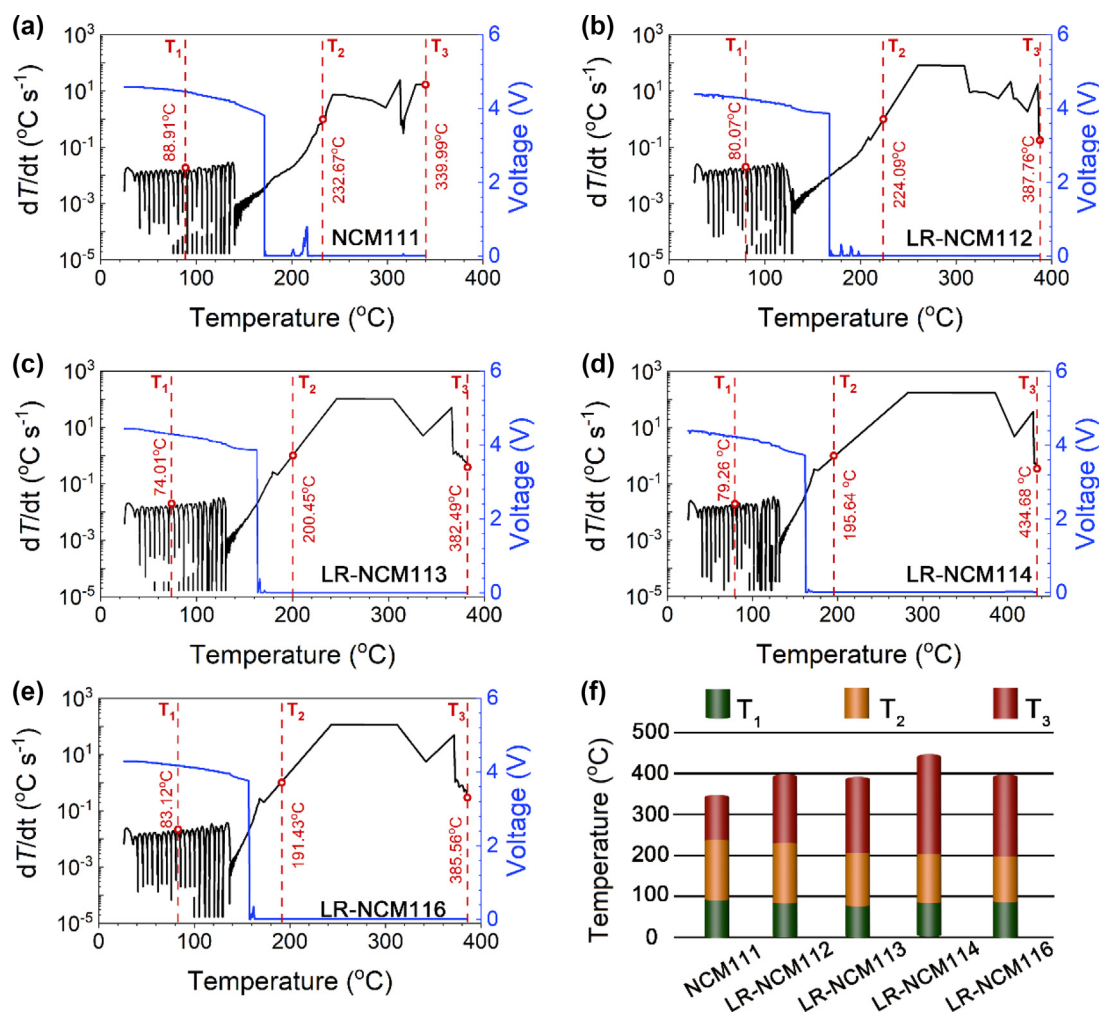

FIGURE 5

Thermal runaway of pouch cells with different cathode materials. (a–e) Comparison of thermal runaway features of (a) NCM111/Graphite, (b) LR-NCM112/Graphite, (c) LR-NCM113/Graphite, (d) LR-NCM114/Graphite and (e) LR-NCM116/Graphite, respectively. (f) Histogram for the comparison of thermal runaway features among different cathodes. The dT/dt –T profiles of these pouch cells obtained from ARC tests, are plotted in logarithmic coordinates. Three temperature parameters, T₁, T₂, and T₃, are defined as the onset temperature of self-heating, the trigger temperature and the maximum temperature of thermal runaway, respectively.

precursors. The synthesis process to use LR-NCM112 and LR-NCM114 precursors (denote as polymorphic LR-NCM113) is depicted in Fig. 6a. Although the Li content keeps identical for both samples (Table S5), the Li amount mixed in both precursors is different from the stoichiometry required for synthesizing LR-NCM112 and LR-NCM114 final products, since the total Li amount is added based on the LR-NCM113 stoichiometry.

Changing the Li content in both precursors has no major influence on the layered structure (Fig. S20). However, a few peaks at higher diffraction angle can be distinguished (Fig. S20b-c), which are attributed to the different lattice parameters. In order to obtain the detailed structural information of the as-prepared polymorphic material, the *Rietveld* refinement was performed on SXRD patterns (Fig. S21). The Li content in TM slab on aver-
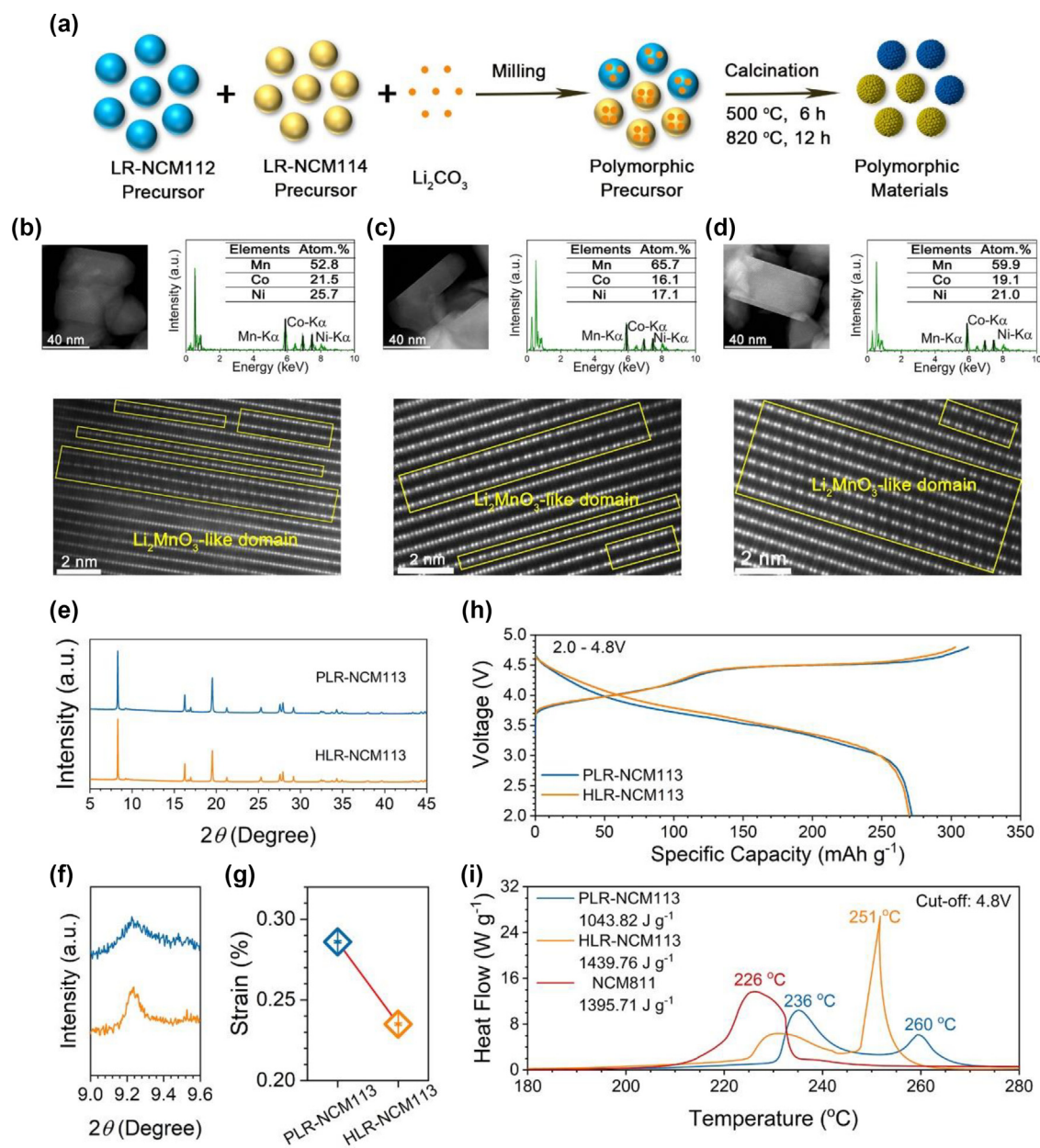

FIGURE 6

Design of high-safety and high-capacity cathode materials. (a) Schematic illustration of the design of the Li-rich polymorphic materials. (b–d) HAADF-STEM images and atomic structure analysis of the intergrowth two domains in [1–10] rhombohedral direction for (b) LR-NCM112 component and (c) LR-NCM114 component in polymorphic material and (d) LR-NCM113 component in homogenous material. The yellow rectangle areas indicate the Li_2MnO_3-like domain. (e-g) The SXRD patterns of PLR-NCM113 and HLR-NCM113 and (f) the enlarged superlattice peaks in SXRD 2θ range of 9–9.6°. (g) Microstrain comparisons between PLR-NCM113 and HLR-NCM113, as determined by refinements of SXRD. (h) Galvanostatic initial charge–discharge profiles at the current density of 25 mA g^{-1} between 2.0 and 4.8 V of the as-prepared PLR-NCM113 and HLR-NCM113 material. The unchanged voltage profiles between PLR-NCM113 and HLR-NCM113 indicate the polymorphic design has no impact on the available discharge capacity. (i) Comparison about the thermal stability of the PLR-NCM113, HLR-NCM113 and NCM811. The less heat release corresponds to an alleviated reaction between oxygen and electrolyte, which implies that the polymorphic design is capable of improving the thermal stability of high-capacity cathode materials.

age of the polymorphic LR-NCM113 (PLR-NCM113) is similar to that of the homogenous LR-NCM113 (HLR-NCM113) based on our *Rietveld* refinement results (Table S6). Note that the particles with different sizes are obtained for the polymorphic material, although they both show a microsphere-like structure, in which the elements of Mn, Co and Ni are distributed uniformly (Figs. S22 and S23). The atomic ratio of Mn, Co, Ni is almost 2:1:1 and 4:1:1 for these two different secondary particles. To reveal the atomic structure, high-angle annular dark-field scanning transmission electron microscopy (HAADF-STEM) was performed. Both $LiTMO_2$-like domains and Li_2MnO_3-like domains coexist in these materials (Fig. 6b–d). Comparing with HLR-NCM113, two components of PLR-NCM113 both show a smaller size of Li_2MnO_3-like domain, indicating the Mn local structure was turned by changing Li content. The change of the Li_2MnO_3-like domain size can also be estimated qualitatively through the superlattice peak in the diffraction pattern. As can be seen in Fig. 6f, a broader superlattice peak is observed in PLR-NCM113, implying the size decrease of Li_2MnO_3-like domain [25]. In addition, a higher microstrain is observed for polymorphic sample induced by the smaller Li_2MnO_3-like domain size (Fig. 6g). As mentioned above, the smaller Li_2MnO_3-like domain size can contribute to an improved O stability [54,60] after the activation of the oxygen redox. The inherently poor O stability in HLR-NCM113 gives rise to the oxygen release and TM migration during heating.

To validate our hypothesis, the electrochemical and thermal measurements were conducted. As can be seen in Fig. 6h, the polymorphic material delivers almost the same capacity as the homogenous version, though the PLR-NCM113 shows a poor initial Coulombic efficiency (ICE). From our Fourier-transformed infrared spectroscopy (FTIR) results (Fig. S24), more carbonate (mainly Li_2CO_3) is formed on the surface of PLR-NCM113 material due to the nonstoichiometric Li amount for both LR-NCM112 and LR-NCM114 precursors. The irreversible surface decomposition of Li_2CO_3 at high potential engenders PLR-NCM113 with a poor ICE [61,62]. Apart from the initial discharge capacity, the cycling and rate performances are compared. As can be seen in Fig. S25a–d, both samples show a similar cycling stability and rate performance, suggesting the polymorphic design does not degrade the electrochemical properties. The structure evolution for cycled materials was also examined through XRD and HADDF-STEM. Although original layered structure is well maintained for electrodes after cycling (Fig. S25e), a thicker disordered layer is formed on the surface of HLR-NCM113, implying a poor structure stability (Fig. S25 f-h). In terms of thermal stability, DSC experiment was conducted on the polymorphic materials after charged at 4.8 V *vs* Li^+/Li^0. Interestingly, two exothermic peaks emerge in DSC profile, which can be attributed to the charged LR-NCM112 and LR-NCM114 components (Fig. 6i). Comparing with HLR-NCM113, although one sharp exothermic peak shift to lower temperature, the decreased heat release (from 1439.8 J g^{-1} to 1043.9 J g^{-1}) implies an improved thermal stability. More surprisingly, a less heat release is obtained for PLR-NCM113 (1043.9 J g^{-1}) even comparing with classical layered $LiNi_{0.8}Co_{0.1}Mn_{0.1}O_2$ (NCM811, 1395.7 J g^{-1}) and NCM111 (1218.2 J g^{-1}) cathodes,

while PLR-NCM113 achieves much higher capacity (Fig. 6i, Figs. S26, S27). In addition, the PLR-NCM113 delivers an improved thermal stability over other classical layered oxides including $LiNi_{0.5}Co_{0.2}Mn_{0.3}O_2$ and $LiNi_{0.90}Co_{0.05}Al_{0.05}O_2$ in terms of less heat generation (Table S7). ARC test was also performed to investigate the influence of polymorphic material on battery safety. Two self-heating processes appear before thermal runaway (Fig. S28). This phenomenon is similar to the two exothermic peaks in DSC curves, which results from the two components in polymorphic material. More importantly, the reduced temperature difference between T_3 and T_1 (ΔT) in ARC test manifests the polymorphic material design enables Li-rich layered cathode to achieve superior electrochemical capacity as well as improved battery stability over classical layered materials.

Conclusions

The in-depth understanding of thermal stability of cathode materials at microscopic and macroscopic level during the operation of batteries is of great importance to formulate engineering strategies to mitigate safety issues for energy storage. In this work, we show that more Mn content in Li-rich layered oxides can contribute to a higher discharge capacity, while it can lead to a faster thermal decomposition reaction accompanying a lower onset temperature of oxygen evolution. This result is greatly ascribed to the change of the Mn local coordination environment. To improve the thermal stability without sacrificing the energy density, compositional design which can optimize Mn local environment is needed. One possible engineering approach by utilizing materials with polymorphism compositions is then demonstrated for achieving reversible and thermally stable anionic redox through control of the Mn coordination environment. Further exploration is needed to fully characterize the precise local ordering difference between the polymorphic materials and the analog materials with homogenous element distribution. The designed polymorphic Li-rich layered oxides exhibit a superior thermal stability, while maintaining a much higher energy density over classical layered oxides, which opens the pathway toward commercialization of Li-rich layered cathode materials for next generation high-energy and high-safety rechargeable batteries.

CRediT authorship contribution statement

Xiao Li: Conceptualization, Formal analysis, Investigation, Methodology, Validation, Visualization, Writing – original draft. **Qingwen Gu:** Investigation, Validation, Resources. **Bao Qiu:** Conceptualization, Investigation, Writing – review & editing, Supervision, Funding acquisition, Project administration. **Chong Yin:** Investigation, Validation. **Zhining Wei:** Investigation, Validation. **Wen Wen:** Methodology, Resources. **Yibin Zhang:** Methodology, Investigation, Validation. **Yuhuan Zhou:** Investigation, Validation. **Han Gao:** Investigation, Validation. **Haoyan Liang:** Investigation, Validation. **Zhilong He:** Methodology, Investigation, Validation. **Minghao Zhang:** Conceptualization, Investigation, Writing – review & editing, Supervision. **Ying Shirley Meng:** Conceptualization,

RESEARCH: Original Research

Writing – review & editing, Supervision. **Zhaoping Liu:** Conceptualization, Writing – review & editing, Supervision, Funding acquisition, Project administration.

Data availability

Data will be made available on request.

Declaration of Competing Interest

The authors declare that they have no known competing financial interests or personal relationships that could have appeared to influence the work reported in this paper.

Appendix A. Supplementary data

Supplementary data to this article can be found online at https://doi.org/10.1016/j.mattod.2022.09.013.

References

[1] N.S. Choi et al., Angew. Chem. Int. Ed. 51 (2012) 9994–10024, https://doi.org/10.1002/anie.201201429.

[2] T.H. Kim et al., Adv. Energy Mater. 2 (2012) 860–872, https://doi.org/10.1002/aenm.201200028.

[3] M. Armand, J.M. Tarascon, Nature 451 (2008) 652–657, https://doi.org/10.1038/451652a.

[4] S.M. Bak et al., ACS Appl Mater Interfaces 6 (2014) 22594–22601, https://doi.org/10.1021/am506712c.

[5] Y.K. Sun et al., J. Am. Chem. Soc. 127 (2005) 13411–13418, https://doi.org/10.1021/ja053675g.

[6] Y.K. Sun et al., Nat. Mater. 11 (2012) 942–947, https://doi.org/10.1038/nmat3435.

[7] Y.K. Sun et al., Nat. Mater. 8 (2009) 320–324, https://doi.org/10.1038/nmat2418.

[8] A. Manthiram, Nat. Commun. 11 (2020) 1550–1558, https://doi.org/10.1038/s41467-020-15355-0.

[9] N. Yabuuchi, T. Ohzuku, J. Power Sources 119–121 (2003) 171–174, https://doi.org/10.1016/s0378-7753(03)00173-3.

[10] B. Qiu et al., Chem. Mater. 29 (2017) 908–915, https://doi.org/10.1021/acs.chemmater.6b04815.

[11] M.M. Thackeray et al., J. Mater. Chem. A 17 (2007) 3112–3125, https://doi.org/10.1039/b702425h.

[12] D.H. Seo et al., Nat. Chem. 8 (2016) 692–697, https://doi.org/10.1038/nchem.2524.

[13] B. Qiu et al., Nat. Commun. 7 (2016) 12108–12131, https://doi.org/10.1038/ncomms12108.

[14] B. Qiu et al., Cell Reports Phys. Sci. 1 (2020), https://doi.org/10.1016/j.xcrp.2020.100028 100028.

[15] S. Hy et al., Energy Environ. Sci. 9 (2016) 1931–1954, https://doi.org/10.1039/c5ee03573b.

[16] M.N. Ates et al., J. Electrochem. Soc. 161 (2014) A290–A301, https://doi.org/10.1149/2.040403jes.

[17] J. Jiang, J.R. Dahn, Electrochim. Acta 50 (2005) 4778–4783, https://doi.org/10.1016/j.electacta.2005.02.031.

[18] H. Konishi et al., Electrochim. Acta 169 (2015) 310–316, https://doi.org/10.1016/j.electacta.2015.03.217.

[19] H. Konishi et al., Electrochim. Acta 186 (2015) 591–597, https://doi.org/10.1016/j.electacta.2015.10.155.

[20] L.G. Wang et al., J. Am. Chem. Soc. 142 (2020) 14966–14973, https://doi.org/10.1021/jacs.0c05498.

[21] T.H. Wu et al., Adv. Mater. 33 (2021) 2001358, https://doi.org/10.1002/adma.202001358.

[22] X. Yang et al., J. Mater. Chem. 22 (2012) 19666–19672, https://doi.org/10.1039/c2jm34259f.

[23] Y. Wang et al., ACS Appl. Mater Interfaces 12 (2020) 8306–8315, https://doi.org/10.1021/acsami.9b21303.

[24] B. Ravel, M. Newville, J. Synchrotron Radiat. 12 (2005) 537–541, https://doi.org/10.1107/S0909049505012719.

[25] C. Yin et al., Mater. Today 51 (2021) 15–26, https://doi.org/10.1016/j.mattod.2021.10.020.

[26] S.M. Bak et al., Chem. Mater. 25 (2013) 337–351, https://doi.org/10.1021/cm303096e.

[27] J.X. Zheng et al., J. Am. Chem. Soc. 138 (2016) 13326–13334, https://doi.org/10.1021/jacs.6b07771.

[28] W.D. Li et al., J. Am. Chem. Soc. 141 (2019) 5097–5101, https://doi.org/10.1021/jacs.8b13798.

[29] J. Zheng et al., Chem. Mater. 27 (2015) 1381–1390, https://doi.org/10.1021/cm5045978.

[30] M. Sathiya et al., Nat. Mater. 12 (2013) 827–835, https://doi.org/10.1038/nmat3699.

[31] J.X. Hou et al., Nat. Commun. 11 (2020) 5100–5110, https://doi.org/10.1038/s41467-020-18868-w.

[32] X. Liu et al., Joule 2 (2018) 2047–2064, https://doi.org/10.1016/j.joule.2018.06.015.

[33] J.L. Shi et al., Nano Res. 10 (2017) 4201–4209, https://doi.org/10.1007/s12274-017-1489-3.

[34] D.C. Chen, W. Kan, G.Y. Chen, Adv. Energy Mater. 9 (2019) 1901255, https://doi.org/10.1002/aenm.201901255.

[35] Y. Lei et al., Adv. Energy Mater. 10 (2020) 2002506, https://doi.org/10.1002/aenm.202002506.

[36] L. Wang, T. Maxisch, G. Ceder, Chem. Mater. 19 (2007) 543–552, https://doi.org/10.1021/cm0620943.

[37] I. Belharouak et al., J. Power Sources 174 (2007) 905–909, https://doi.org/10.1016/j.jpowsour.2007.06.092.

[38] A.R. Armstrong et al., J. Am. Chem. Soc. 128 (2006) 8694–8698, https://doi.org/10.1021/ja062027+.

[39] D.Y.W. Yu et al., J. Electrochem. Soc. 156 (2009) A417–A424, https://doi.org/10.1149/1.3110803.

[40] K.W. Nam et al., Adv. Funct. Mater. 23 (2013) 1047–1063, https://doi.org/10.1002/adfm.201200693.

[41] X. Liu et al., J. Am. Chem. Soc. 142 (2020) 19745–19753, https://doi.org/10.1021/jacs.0c09961.

[42] E.Y. Hu et al., Nat. Energy 3 (2018) 690–698, https://doi.org/10.1038/s41560-018-0207-z.

[43] Y. Wei et al., J. Am. Chem. Soc. 137 (2015) 8364–8367, https://doi.org/10.1021/jacs.5b04040.

[44] B.J. Hwang et al., Chem. Mater. 15 (2003) 3676–3682, https://doi.org/10.1021/cm030299v.

[45] Y.X. Li et al., Energy Stor. Mater. 35 (2021) 99–107, https://doi.org/10.1016/j.ensm.2020.11.013.

[46] P.F. Liu et al., J. Phys. Chem. Lett. 10 (2019) 2202–2207, https://doi.org/10.1021/acs.jpclett.9b00419.

[47] Y.W. Tsai et al., Chem. Mater. 17 (2005) 3191–3199, https://doi.org/10.1021/cm048027v.

[48] N. Yabuuchi et al., Proc Natl Acad Sci U S A 112 (2015) 7650–7655, https://doi.org/10.1073/pnas.1504901112.

[49] N. Yabuuchi, Chem. Rec. 19 (2019) 690–708, https://doi.org/10.1002/tcr.201800089.

[50] U. Maitra, A.K. Das, ACS Appl. Energy Mater. 5 (2022) 4522–4535, https://doi.org/10.1021/acsaem.1c04112.

[51] X.N. Feng et al., Appl. Energy 246 (2019) 53–64, https://doi.org/10.1016/j.apenergy.2019.04.009.

[52] D.S. Ren et al., Appl. Energy 228 (2018) 633–644, https://doi.org/10.1016/j.apenergy.2018.06.126.

[53] X. Feng et al., Energy Stor. Mater. 10 (2018) 246–267, https://doi.org/10.1016/j.ensm.2017.05.013.

[54] J. Hwang et al., Adv. Mater. 32 (2020) 2001944, https://doi.org/10.1002/adma.202001944.

[55] J. Hwang et al., Adv. Mater. 33 (2021) 2100352, https://doi.org/10.1002/adma.202100352.

[56] Y. Li et al., Energy Stor. Mater. 45 (2022) 422–431, https://doi.org/10.1016/j.ensm.2021.12.003.

[57] E. Lee, K.A. Persson, Adv. Energy Mater. 4 (2014) 1400498, https://doi.org/10.1002/aenm.201400498.

[58] W.B. Hua et al., Nat. Commun. 10 (2019) 5365–5375, https://doi.org/10.1038/s41467-019-13240-z.

[59] W. Hua et al., Adv. Energy Mater. 9 (2019) 1803094, https://doi.org/10.1002/aenm.201803094.

[60] S. Myeong et al., Nat. Commun. 9 (2018) 3285–3294, https://doi.org/10.1038/s41467-018-05802-4.

[61] Z. Zhuo et al., Joule 5 (2021) 975–997, https://doi.org/10.1016/j.joule.2021.02.004.

[62] N. Yabuuchi et al., J. Am. Chem. Soc. 133 (2011) 4404–4419, https://doi.org/10.1021/ja108588y.